ARTICLE IN PRESS

Journal of Fluids and Structures xxx (xxxx) xxx

Contents lists available at ScienceDirect

Journal of Fluids and Structures

journal homepage: www.elsevier.com/locate/jfs

Large amplitude cross-stream sphere vibration generated by applied rotational oscillation

Anchal Sareen *, Jisheng Zhao, John Sheridan, Kerry Hourigan, Mark C. Thompson

Fluids Laboratory for Aeronautical and Industrial Research (FLAIR), Department of Mechanical and Aerospace Engineering, Monash University, Melbourne, VIC 3800, Australia

ARTICLE INFO

Article history:
Received 2 November 2018
Received in revised form 22 February 2019
Accepted 27 March 2019
Available online xxxx

Keywords:
Flow-induced vibration
Rotation
VIV
Lock-in

ABSTRACT

A new class of vibrations has been discovered where the vibrations are induced by forced sinusoidal rotary oscillation of a sphere. They have been termed *Rotary-Induced Vibrations* (RIV). RIV is observed only for selected forcing parameters, where the vibrations are locked to the forcing frequency. For these cases, the vibration amplitude increases monotonically with an increase in U^*, similar to a galloping response. However, unlike the galloping response which is typically observed for high flow velocities and is generated by lift caused by body asymmetry, RIV is observed for the entire fundamental synchronisation regime of a sphere. RIV is found to be driven by vortex shedding as well as the imposed rotary oscillation, which causes an oscillatory Magnus force. As is typical of forced oscillations, the band of forcing frequencies that leads to RIV becomes wider with forcing amplitude, and is centred on the resonant condition for which the forcing frequency matches the natural system frequency. At a reduced velocity of 20, which is approximately 3 times the resonant reduced velocity, the vibration amplitude was more than 50% greater than the unforced case.

1. Introduction

Flow-induced vibration (FIV) has been an especially active area of research over the last four decades. This has resulted in a number of literature reviews focused on understanding the underlying mechanisms (e.g. Sarpkaya (2004), Williamson and Govardhan (2004), Gabbai and Benaroya (2005), Païdoussis et al. (2010)). For some applications, e.g., heat exchangers, oil risers, offshore structures and bridges, FIV is undesirable as it can cause severe structural fatigue and damage. Hence, many past studies have focused on suppressing large-amplitude vibrations. Choi et al. (2008) provides a comprehensive review on various active and passive control methods that have been employed.

On the other hand, some researchers have exploited energetic vibration to harness flow energy (e.g., Barrero-Gil et al. (2012), Wang et al. (2017) and Soti et al. (2018)). For both sets of applications, it is crucial to be able to predict the structural vibration response so that suitable control or energy-harvesting methods can be employed.

Recently, VIV control using rotary oscillation has gained increased attention. A numerical study by Du and Sun (2015) and an experimental study by Wong et al. (2018) explored the potential of imposed rotary oscillation to control vortex-induced vibration (VIV) of a cylinder. A very recent study by Sareen et al. (2018b) examined the potential of rotary oscillation to control VIV of a sphere. These studies demonstrated that when the imposed forcing frequency, f_r, is close to

* Corresponding author.
E-mail address: anchal.sareen@monash.edu (A. Sareen).

https://doi.org/10.1016/j.jfluidstructs.2019.03.025
0889-9746/

Please cite this article as: A. Sareen, J. Zhao, J. Sheridan et al., Large amplitude cross-stream sphere vibration generated by applied rotational oscillation. Journal of Fluids and Structures (2019), https://doi.org/10.1016/j.jfluidstructs.2019.03.025.

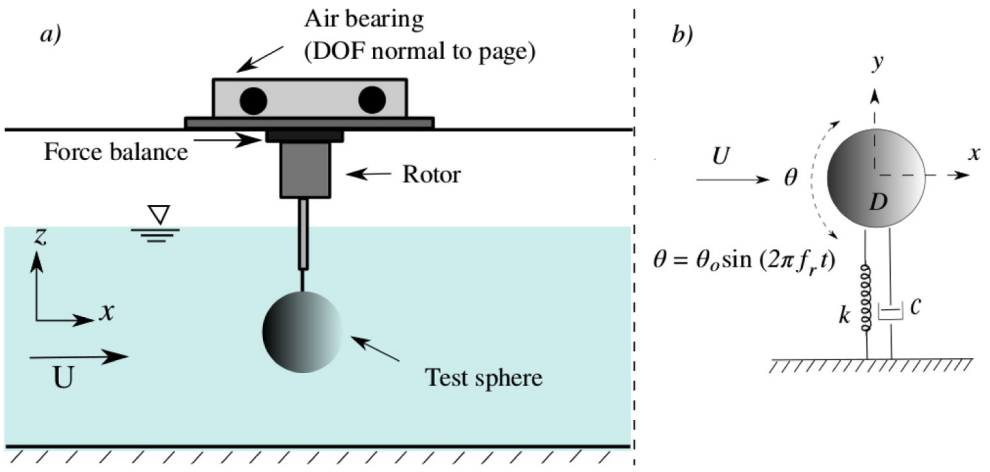

Fig. 1. (a) Schematic of the experimental set-up. (b) Definition sketch of the current fluid–structure interaction problem consisting of a 1-DOF system constrained to move only in the cross-flow direction. Here, D is the sphere diameter, U is the free-stream velocity, k the spring constant, c the structural damping, and θ the imposed angular displacement.

(but not equal to) f_{nw} (natural frequency of the system), then the vortex shedding frequency, f_{sh}, locks on to f_r instead of f_{nw}, thereby possibly inhibiting resonance and suppressing vibration. This phenomenon is called lock-on, or in this case, *rotary* lock-on.

Of particular interest here is the response that is observed for certain forcing parameters, for which the vibration amplitude increases monotonically with reduced velocity (normalised flow velocity). Previously, Sareen et al. (2018b) reported a monotonically increasing vibration response for a sphere for $f_R = f_r/f_{\mathrm{nw}} \sim 1$ at α_R. Here, α_R is forcing amplitude ratio defined as the ratio of the equatorial surface velocity amplitude of the sphere to the freestream speed. For those control parameters, they found that vibrations are always locked-on to the forcing frequency. This monotonically increasing vibration response was termed *rotary-induced vibration* (RIV). However, Sareen et al. (2018a) reported RIV only for an amplitude ratio of $\alpha_R = 1$ for two cases with forcing frequency ratios very close to unity. In that paper, it was not explored how the characteristics of RIV change with amplitude ratio. Does RIV persist for even smaller amplitude ratios? How does the saturation amplitude increase with an increase in the amplitude ratio, and how does the forcing frequency range for occurrence change? This current study focuses on rotary-induced vibration to characterise its behaviour for amplitude ratio between $0 \leqslant \alpha_R \leqslant 2$ to determine the frequency ratio for occurrence. Specifically, the current study maps out the parameter space where RIV is observed and provides a more detailed analysis and characterisation than previously undertaken.

2. Experimental methodology

The experiments were carried out in the recirculating free-surface water channel of the Fluids Laboratory for Aeronautical and Industrial Research (FLAIR) at Monash University, Australia. The test section of the channel is 600 mm wide, 800 mm deep and 4000 mm long. The free-stream turbulence level was less than 1% for the current experiments. A uniform density spherical acrylic ball with a smooth polished surface was used for the experiments. The diameter of the sphere was $D = 80$ mm (accurate to within $\pm$ 200 μm).

The rotary motion was provided using a miniature low-voltage micro-stepping motor with a resolution of 25 000 steps/revolution. The rotary oscillation was monitored using a digital optical rotary encoder with a resolution of 4000 counts/revolution. More details of the rotary device can be found in the studies of Wong et al. (2017, 2018) and Zhao et al. (2018b). The sphere cross-stream displacement was measured using a linear encoder with a resolution of 1 μm. For each data set, the signal was acquired at a sampling frequency of 100 Hz for more than 100 vibration cycles. A schematic of the current problem set-up is given in Fig. 1. The sphere was free to move in the direction transverse to the flow. An air bearing rig was employed to provide the near-frictionless motion, which has been validated and used in many related FIV studies in the FLAIR group (e.g. Zhao et al., 2018a,b, 2019a,b). Further details of the setup can be found in Sareen et al. (2018b).

The sphere vibration response is often characterised using the amplitude ratio A^* and frequency ratio f^* as a function of reduced velocity U^*. Here, $A^* = \sqrt{2}y_{rms}/D$, $f^* = f/f_{\mathrm{nw}}$ and $U^* = U/(f_{\mathrm{nw}}D)$, where y_{rms} is the root-mean-square measure of the sphere oscillation signal in the transverse direction, f is the oscillation frequency, U is the free-stream velocity and D is the sphere diameter. The other important non-dimensional parameters are C_y, defined as $C_y = F_y/(\frac{1}{8}\rho U^2 \pi D^2)$, and $f^*_{C_y}$, defined as $f^*_{C_y} = f_{C_y}/f_{\mathrm{nw}}$. Here, F_y is the total transverse force acting on the sphere, ρ is the fluid density and f_{C_y} is the dominant frequency of the transverse force.

Please cite this article as: A. Sareen, J. Zhao, J. Sheridan et al., Large amplitude cross-stream sphere vibration generated by applied rotational oscillation. Journal of Fluids and Structures (2019), https://doi.org/10.1016/j.jfluidstructs.2019.03.025.

The rotary oscillation motion of the sphere is characterised by the forcing frequency ratio, f_R, and the forcing amplitude ratio, α_R. As introduced previously, f_R is defined as the ratio of forcing frequency, f_r, to the natural frequency of the system, f_{nw}, as

$$f_R = f_r/f_{\mathrm{nw}}. \tag{1}$$

The other parameter, α_R, is expressed as the ratio of the maximum tangential velocity of the sphere surface to the free-stream velocity U, as

$$\alpha_R = \frac{D\dot{\theta}_{max}}{2U}, \tag{2}$$

where $\dot{\theta}_{max}$ is the maximum angular velocity of the sphere.

The equation governing cross-flow motion of the sphere can be written as

$$m\ddot{y} + c\dot{y} + ky = F_y \tag{3}$$

where F_y is the fluid force in the transverse direction, m is the total oscillating mass of the system, y is the displacement of the sphere in the transverse direction, c is the structural damping of the system, and k is the spring constant. As a first approximation, it is often assumed that $F_y(t)$ and $y(t)$ are both sinusoidal and can be represented as

$$y(t) = A\sin(2\pi ft), \tag{4}$$

$$F_y(t) = F_o\sin(2\pi ft + \phi_{\mathrm{total}}). \tag{5}$$

Based on suggestions by Lighthill (1986), Govardhan and Williamson (2000) and others, the total transverse force (F_y) can be split into a potential force (comprising the potential added-mass force, F_p) and a vortex force (due to vorticity dynamics, F_v). From the potential theory, the instantaneous potential force acting on the sphere can be expressed as

$$F_p(t) = -C_A m_d\ddot{y}(t), \tag{6}$$

where C_A is the potential flow added mass coefficient (0.5 for a sphere), m_d is the displaced fluid mass and $\ddot{y}$ is the acceleration in the transverse direction. Thus, the vortex force F_v can be computed from

$$F_v = F_y - F_p. \tag{7}$$

If all the forces are normalised by $(\frac{1}{2}\rho U^2\pi D^2/4)$, this reduces to

$$C_{\mathrm{vortex}}(t) = C_y(t) - C_{\mathrm{potential}}(t). \tag{8}$$

Hence, the equation of motion can also be written as

$$(m + m_A)\ddot{y} + c\dot{y} + ky = F_{vortex}\sin(\omega t + \phi_{\mathrm{vor}}). \tag{9}$$

The vortex phase ϕ_{vor}, first introduced by Govardhan and Williamson (2000), is the phase difference between the vortex force $C_{\mathrm{vortex}}(t)$ and the body displacement $y(t)$. The more conventionally used total phase ϕ_{total} is the relative phase angle of the total force C_y to the body displacement $y(t)$.

The sinusoidal rotary motion imposed on the sphere can be expressed as

$$\theta(t) = \theta_o\sin(2\pi f_r t + \phi_{\mathrm{rot}}), \tag{10}$$

where θ is time-dependent imposed angular displacement, θ_o is maximum angular displacement and f_r is the forcing frequency and ϕ_{rot} is the phase difference between the sphere displacement and the imposed sinusoidal rotary motion. The theory presented in this section assumes that the signals are all purely sinusoidal at a fixed frequency. The system dynamics is more complex in reality, of course, with how well the displacement and force signals actually satisfy those assumptions depending on control parameters. In any case, it is possible to define instantaneous phases using a Hilbert transform (e.g. Khalak and Williamson, 1999; Zhao et al., 2014a,b), which helps to define how the signals relate to one another both instantaneously and on average.

Readers should be mindful here that in the current problem, the sphere experiences a Magnus force due to rotation, which can be partially described by potential theory. However, the maximum mean lift coefficient experienced by a sphere tends to be limited to $\sim$ 0.5, while potential theory predicts it to vary as 2α (Rubinow and Keller, 1961). Moreover, there will be a time lag in the generation of the Magnus force after the sphere rotational velocity is increased, since it is transmitted through viscous diffusion, that will contribute to complex dynamics. In addition, it can be expected there will be contributions to the vortex force from the vorticity induced by the oscillatory sphere rotation as well as from natural vortex shedding depending on the frequency ratio of these two phenomena. Thus, unlike the unforced case, the *vortex force* here may need to account for these contributions, i.e., natural vortex shedding, vortex shedding associated with oscillatory rotational oscillation and a Magnus component that can be associated with bound vorticity. Nevertheless, Eq. (9) should still be useful to understand the current problem and may help shed light into the dynamics.

Please cite this article as: A. Sareen, J. Zhao, J. Sheridan et al., Large amplitude cross-stream sphere vibration generated by applied rotational oscillation. Journal of Fluids and Structures (2019), https://doi.org/10.1016/j.jfluidstructs.2019.03.025.

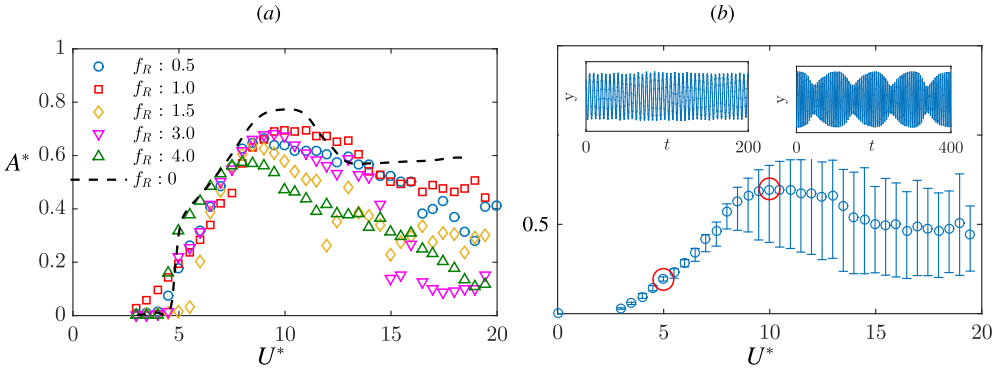

Fig. 2. (a) Vibration response of a sphere for various f_R values at an amplitude ratio of $\alpha_R = 0.5$. (b) Vibration response for a sphere for $f_R = 1$ and $\alpha_R = 0.5$. The 'error bars' are bounded by the means of the top 10% and bottom 10% peaks of the sphere vibration. Time traces of the sphere displacement are also shown for two selected cases of $U^* = 5$ (left) and $U^* = 10$ (right).

3. Sphere vibration response without rotary oscillation

The Reynolds number in the current study varies in the range $3840 \leq \mathrm{Re} \leq 25\,600$. For a stationary sphere at such high Reynolds numbers, vortex loops emanate at a Strouhal frequency of $St = f_{\mathrm{sh}}D/U \approx 0.2$, where f_{sh} is the vortex shedding frequency. If a sphere is mounted elastically in the transverse direction, resonance or lock-in kicks in when the vortex shedding frequency is equal to the natural frequency of the system, i.e, $U^* = 1/St \approx 5$ (See the dashed curve of Fig. 2). Once lock-in kicks in, the sphere continues to experience large vortex-induced vibration (VIV) for a wide range of reduced velocities. The vibration amplitude increases as the response moves through sphere vibration modes I to II, reaching plateau values for mode III at higher flow velocities. The sphere response with no imposed rotation is discussed in detail in studies by Govardhan and Williamson (2005) and Sareen et al. (2018a,c). During VIV, the vortex shedding as well as the sphere vibration are locked to the natural frequency of the system for low mass-damping systems. In the following discussion, this will be referred as the 'natural vortex shedding' or the 'natural shedding frequency'.

Sareen et al. (2018b) reported deviation of the vortex shedding frequency from the natural frequency of the system under imposed rotary oscillation. They demonstrated that under the influence of rotary motion of the sphere, the timing of vortex formation changes leading to deviation of the vortex shedding frequency from the natural frequency towards the forcing frequency f_r. As it will be shown in the following discussion, the vortex shedding may show only a single frequency at f_r or both frequencies of f_r and f_{nw} or may also show a more complex behaviour, with additional frequency content including higher harmonics of the forcing frequency.

4. Effect of imposed rotary oscillation

Fig. 2 shows the sphere response for a selection of f_R values for an amplitude ratio of $\alpha_R = 0.5$. As evident from Fig. 2(a), the sphere vibration response resembles the typical response curve observed for a non-rotating sphere, whereby the response increases gradually from mode I to mode II. However, there is a significant reduction in the vibration amplitude at higher reduced velocities ($U^* \geq 10$). Large variations in the instantaneous vibration amplitude are also observed for higher $U^* \gtrsim 8$, as depicted in 2(b). Conversely, time traces of the sphere displacement show that the vibration remains periodic for $U^* \lesssim 8$. However, the time trace shows beating at a very low frequency for higher reduced velocity of $U^* > 8$.

Similar response curves were also observed for $\alpha_R = 0.25$ (although not shown here). This leads to a conclusion that RIV is not observed for low forcing amplitude ratios (at least over the range of f_R tested in this study).

In order to see the effect of forcing amplitude ratio, higher values of $\alpha_R = 1$ and 2 were tested. Fig. 3 shows the sphere vibration amplitude response for various f_R values for a high forcing amplitude ratio of $\alpha_R = 2$. As also demonstrated in Sareen et al. (2018b), the sphere exhibits a rich response showing characteristically different response curves depending on the f_R value. In Fig. 3, $f_R = 1$, $f_R = 1.2$ and $f_R = 1.5$ show a monotonic increase in the vibration amplitude with U^*. These three cases are examples of *rotary-induced vibration*. For $f_R = 4$, the sphere exhibits lock-in or resonance followed by suppression of vibrations. There is no RIV in this case. On the other hand, $f_R = 0.5$ is an interesting case exhibiting VIV followed by rotary lock-on at higher U^*. In the following sections, RIV cases will be discussed in more detail.

5. Characteristic behaviour and the mechanism of RIV

In this section, selected cases of RIV are presented and their characteristic behaviour is discussed. One of the characteristic features of RIV is the monotonic (approximately linear) increase of the vibration amplitude with increasing

Please cite this article as: A. Sareen, J. Zhao, J. Sheridan et al., Large amplitude cross-stream sphere vibration generated by applied rotational oscillation. Journal of Fluids and Structures (2019), https://doi.org/10.1016/j.jfluidstructs.2019.03.025.

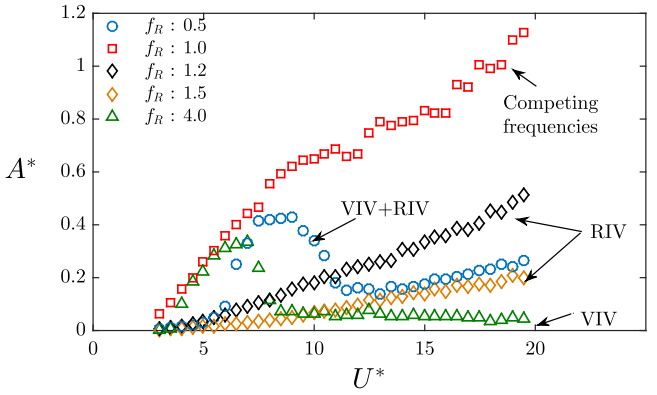

Fig. 3. Sphere vibration response as a function of reduced velocity for various frequency ratios at a high forcing amplitude ratio of $\alpha_R = 2$. For this α_R value, the sphere exhibits various characteristically different FIV responses depending on f_R.

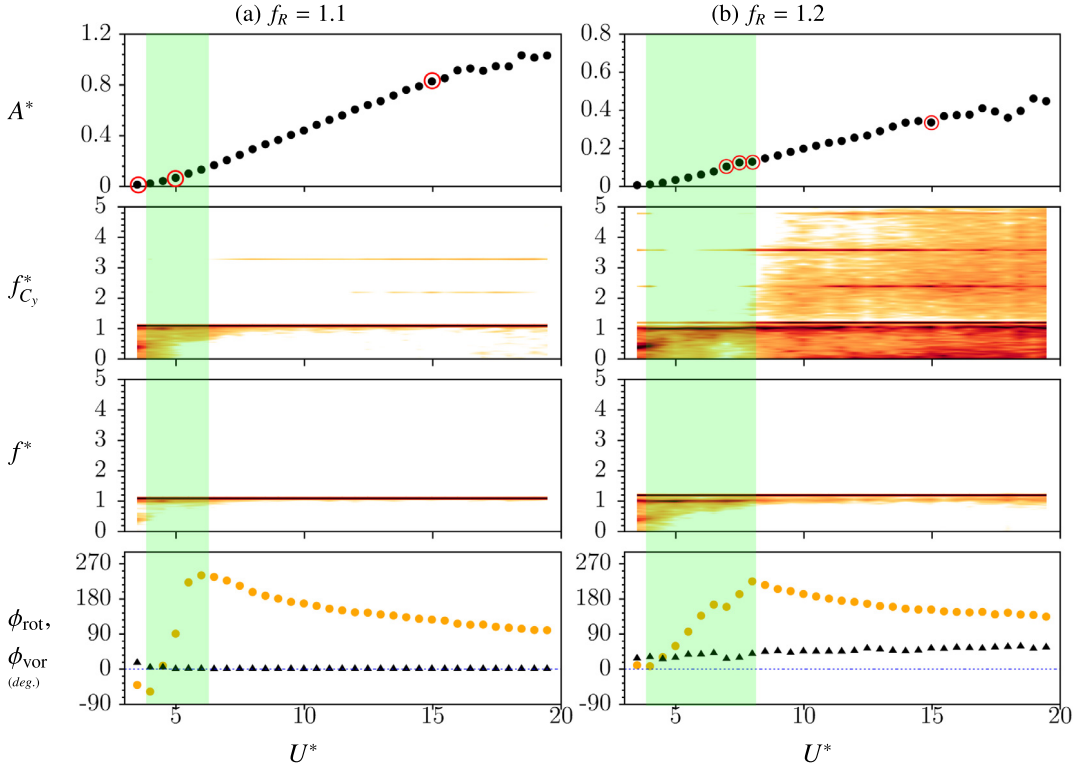

Fig. 4. The RIV response of a sphere under imposed rotary oscillation at a forcing amplitude ratio of $\alpha_R = 1$ for frequency ratios of $f_R = 1.1$ (a) and $f_R = 1.2$ (b). The correlated phases and PSD contours of $f^*_{C_y}$ and f^* are also shown below. Circular symbols in the phase plot represent ϕ_{rot}, and triangular symbols represent ϕ_{vor}. The green-shaded region highlights the region where ϕ_{rot} increases. Time traces for the marked symbols in (a) and (b) are shown in Figs. 5 and 6, respectively. (For interpretation of the references to colour in this figure legend, the reader is referred to the web version of this article.)

reduced velocity. This trait is similar to the galloping response known for non-circular bluff bodies. Galloping is observed at high flow velocities and is essentially a low frequency phenomenon (Blevins (1990), Nemes et al. (2012) and Zhao et al. (2014b)). In addition, it is usually associated with high mass ratio systems. In the present case, RIV can also be observed in the same parameter space in which resonance is observed in the absence of rotary oscillation as well as at higher reduced velocities.

Fig. 4(a) shows response quantities for $f_R = 1.1$ at an amplitude ratio of $\alpha_R = 1$. As evident from the figure, the vibration amplitude increases monotonically as the reduced velocity is increased. The power spectral density (PSD) contour plot of the sphere displacement shows the dominant frequency at the forcing frequency. It is interesting to note

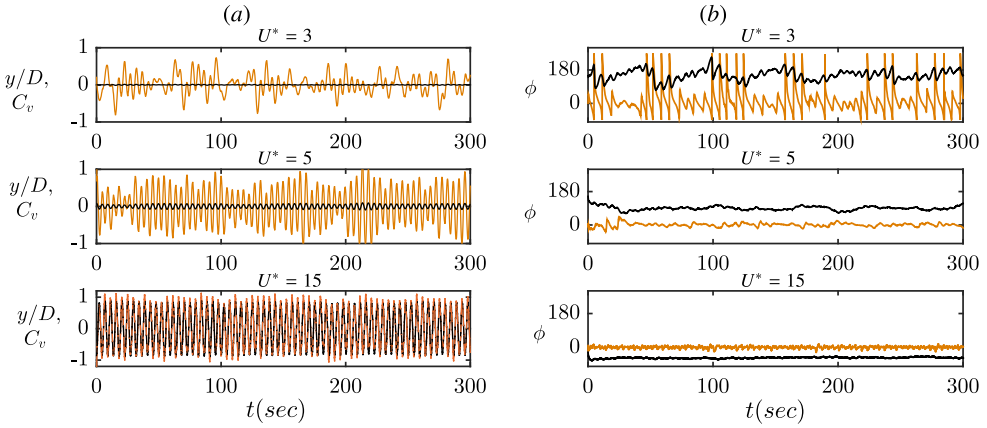

Fig. 5. (a) Time trace of the sphere displacement (black colour) and coefficient of the vortex force C_v (orange). (b) Time trace of the instantaneous phases ϕ_{rot} (black) and ϕ_{vor} (orange). The time traces are shown for $U^* = 3$, 5, and 15 (also marked in Fig. 4(a)) for an amplitude ratio and frequency ratio of $\alpha = 1$ and $f_R = 1.1$, respectively. (For interpretation of the references to colour in this figure legend, the reader is referred to the web version of this article.)

here that the phase difference between the vortex force and the sphere displacement (ϕ_{vor}) remains zero for the entire range of U^*. It appears that the vortex shedding assists to sustain these vibrations.

On the other hand, the PSD contour plot of $C_{y_{rms}}$ also shows a dominant frequency at the forcing frequency. Of interest is the sudden jump observed in the phase difference between the imposed rotary oscillation and the sphere displacement (ϕ_{rot}). All the RIV responses observed in the current study exhibited a monotonic decrease of ϕ_{rot} with increasing reduced velocity beyond the resonant region. As indicated, due to rotary oscillation of the sphere, an oscillating Magnus force is generated in the transverse direction, which presumably also contributes to sphere oscillation along with direct forcing from vortices shedding into the wake.

The time traces of the instantaneous phases calculated using a Hilbert transform are shown in Fig. 5. For very low reduced velocity of $U^* = 3$, large fluctuations in ϕ_{vor} are evident. The time trace of C_v also shows large variations with time. Beyond this U^* where the oscillation amplitude becomes significant, both phases, ϕ_{vor} and ϕ_{rot}, remain fairly constant for $U^* = 5$. For very high reduced velocity of $U^* = 15$, C_v and y/D are highly periodic and both the phases remain steady. These findings show the consistent constant phasing between the different signals that occurs for this near resonant case. At high U^*, it also appears to indicate that the vortex forcing is caused by vortices shed at the forcing frequency rather than the natural shedding frequency.

For $f_R = 1.2$ and $\alpha_R = 1$, the PSD contour plot of the transverse force coefficient shows broad frequency content for $U^* \geq 8$ (Fig. 4(b)). Distinct higher harmonics (second and third harmonics) of the forcing frequency are also clearly evident. The sphere displacement, however, remains locked to the forcing frequency for the entire range of reduced velocities. A close examination of the instantaneous phases (ϕ_{rot} and ϕ_{vor}, see Fig. 6) reveals that there is transition in the signal at $U^* = 8$ (see Fig. 6(b)). At this particular reduced velocity, the displacement signal shows beating for an initial period of time and subsequently undergoes a transition to where the displacement and applied forcing become locked. However, when that occurs, the vortex phase is far from constant. This may suggest that normal vortex shedding is occurring or at least varying on top of the vortex shedding associated with the oscillating rotational motion of the sphere.

The transition between these two types of behaviour is also evident in the time traces of C_v and y/D shown in Fig. 6(a). Interestingly, the large variation in the mean amplitude of the lift coefficient observed in the different regions does not translate to the sphere displacement, as evident from the time trace of y/D in the figure (especially for $U^* = 8$). Although there is a phase shift in ϕ_{rot} and ϕ_{vor} at $U^* = 7.5$, the sphere vibration amplitude hardly shows any trace of this phase shift and keeps increasing smoothly with increasing reduced velocity (see Fig. 4(b)). However, the PSD plot of the lift force coefficient shows a drastic change in the frequency content for $U^* \geq 8$. Intriguingly, ϕ_{vor} is not maintained at zero but varies between ≈ 40 and 60°, unlike the previous case of $f_R = 1.1$. Note here that the RIV response for $f_R = 1.2$ is also characterised by a sudden jump in ϕ_{rot}.

Fig. 7(b) shows another example of RIV for $f_R = 1.5$ and $\alpha_R = 2$. For this case, ϕ_{vor} is out of phase with the displacement for $U^* \approx 6 - 12$ (see highlighted region). Interestingly, outside of that region, both the displacement and lift signals show clear frequency content at both the natural and forcing frequencies. Despite this, there is a smooth variation in the amplitude response with U^* over the entire range.

An interesting case is when the dominant frequencies of the system are equal, i.e. $f_R = 1$. This is shown in Fig. 7(a). The sphere displacement as well as the transverse force show a clean frequency response. The vortex force is in phase with the sphere displacement for the entire range of U^*. The rotary oscillation enhances the sphere vibration with increasing reduced velocity as ϕ_{rot} decreases from 180° to 90° for $U^* \lesssim 10$. However, for $U^* \geq 10$, ϕ_{rot} remains fixed and the

Please cite this article as: A. Sareen, J. Zhao, J. Sheridan et al., Large amplitude cross-stream sphere vibration generated by applied rotational oscillation. Journal of Fluids and Structures (2019), https://doi.org/10.1016/j.jfluidstructs.2019.03.025.

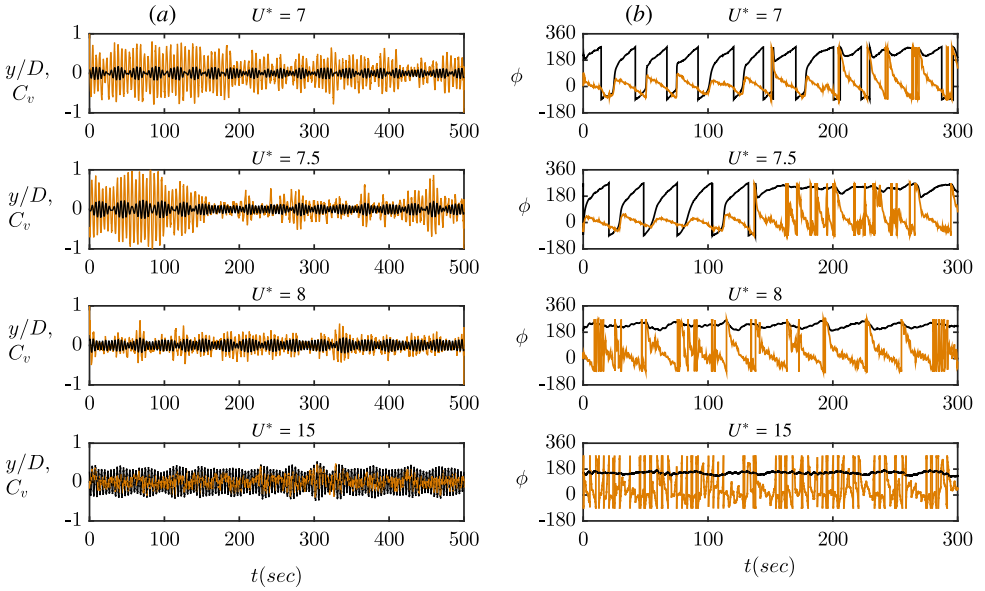

Fig. 6. (a) Time trace of the sphere displacement (black colour) and coefficient of the vortex force C_v (orange). (b) Time trace of the instantaneous phases ϕ_{rot} (black) and ϕ_{vor} (orange). The time traces are shown for $U^* = 7$, 7.5, 8 and 15 (also marked in Fig. 4(b)) for an amplitude ratio and frequency ratio of $\alpha = 1$ and $f_R = 1.2$, respectively. (For interpretation of the references to colour in this figure legend, the reader is referred to the web version of this article.)

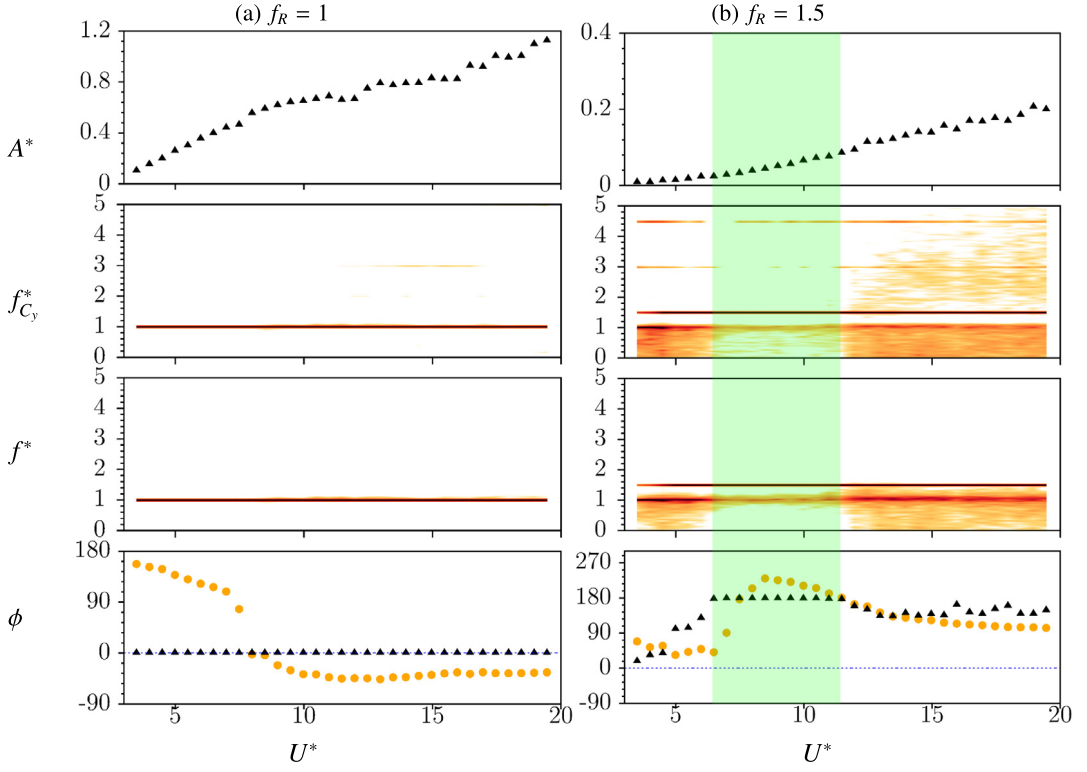

Fig. 7. The RIV response of a sphere under imposed rotary oscillation for (a) $f_R = 1, \alpha_R = 2$ and (b) $f_R = 1.5, \alpha_R = 2$. Circular symbols in the phase plot represent ϕ_{rot}, and triangular symbols represent ϕ_{vor}. The highlighted region for $f_R = 1.5$ shows RIV observed for $\phi_{\text{total}} = 180°$. The green-shaded region highlights the region where ϕ_{vor} is fixed at 180°. (For interpretation of the references to colour in this figure legend, the reader is referred to the web version of this article.)

Please cite this article as: A. Sareen, J. Zhao, J. Sheridan et al., Large amplitude cross-stream sphere vibration generated by applied rotational oscillation. Journal of Fluids and Structures (2019), https://doi.org/10.1016/j.jfluidstructs.2019.03.025.

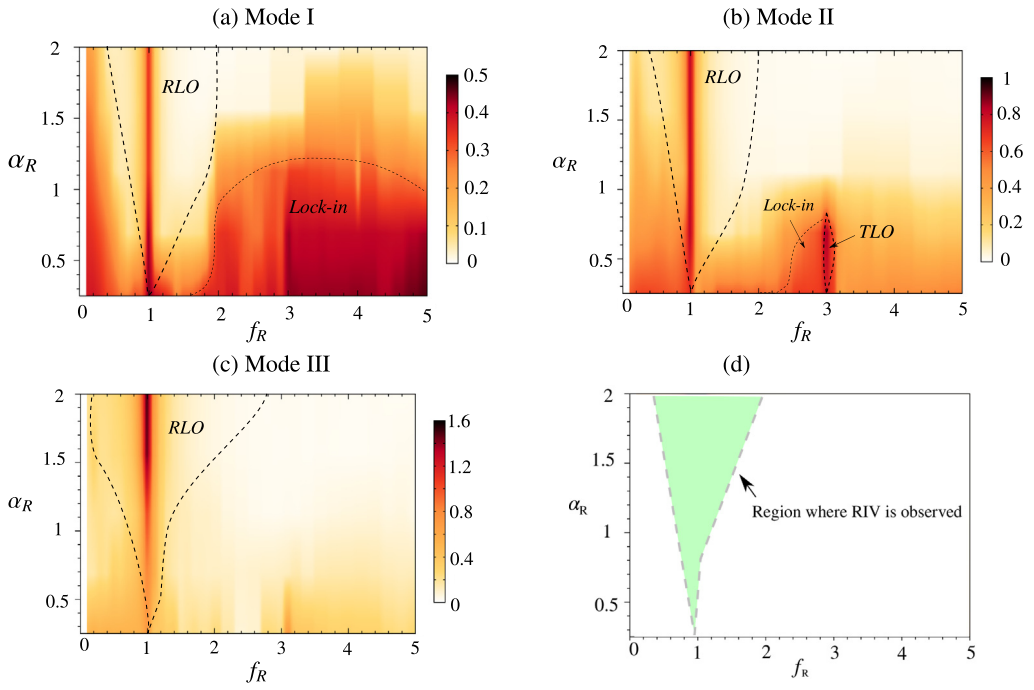

Fig. 8. Plots showing the contours of A^* as a function of α_R and f_R in mode I (a), mode II (b) and mode III (c). Here (d) highlights the region in α_R–f_R parameter space, where RIV is observed based on the intersection of rotary lock-on regions shown in (a), (b) and (c). Note that *RLO* indicates rotary lock-on, and *TLO* tertiary lock-on.
Source: In addition, please note that figures (a), (b) and (c) have been reproduced from Sareen et al. (2018b).

vibration amplitude does not increase as rapidly as for $U^* \lesssim 10$. The maximum vibration amplitude recorded in this case is at the highest reduced velocity tested of $U^* = 20$. In that case, the recorded amplitude was more than 50% higher than the maximum amplitude seen in the unforced case ($\sim 0.80 : 1.2$).

Sareen et al. (2018b) performed extensive wake measurements and observed no significant change in the dominant wake structures in the lock-on regions. However, they reported a change in the timing of vortex formation consistent with the change in ϕ_{vor}. In the present case, since the sphere vibrations are always locked-on to the forcing frequency in RIV, one can expect that there will not be any significant change in the dominant vortex structures in the sphere wake. However, the rotary motion of the sphere induces vortex shedding at the forcing frequency. Therefore, there should be a change in the timing of the vortex formation.

In the sense that the forcing is externally applied, rather that induced by body or flow asymmetry, rotary-induced vibrations might be better compared to wake-induced vibrations (WIV) rather than galloping. Assi et al. (2010) reported WIV for an elastically mounted cylinder placed downstream of a fixed cylinder. In their study, the elastically mounted cylinder exhibited only WIV, only VIV, combined WIV and VIV, and separated WIV and VIV, depending on the cylinders' separation (that essentially changes the phase difference between the two vortex sheddings). In any case, the forcing of the second cylinder is a result of the transversely oscillating pressure as the positive and negative wake vortices from the first cylinder advect downstream past the second cylinder. The case here is perhaps more complicated because of the various different components of the vortex force discussed in Section 2.

These findings are very interesting from the viewpoint of energy extraction applications. If we know the favourable forcing parameters, we can achieve enhanced sphere vibrations of the order of 1.5 sphere diameters for a wide range of flow velocities. Of course, it is possible that even higher amplitudes could be achieved at higher reduced velocities. It is also important to predict such vibrations even for control applications, where the aim is to suppress such vibrations. It is crucial to know the parameter space of $\alpha_R - f_R$, where RIV is observed so as to avoid those conditions. By examining the sphere response frequency as a function of f_R for each fixed α_R in the current experiments, we can estimate the region where RIV is observed in the $\alpha_R - f_R$ parameter space. When reduced velocity is progressively increased, monotonically increasing vibration amplitude (RIV) is observed only in those cases where there is rotary lock-on in all the three modes of sphere vibrations. Based on this criterion, a region can be mapped out in $\alpha_R - f_R$ parameter space, where there is lock-on in all the three modes. Such a region has been highlighted in Fig. 8. Fig. 8 shows the approximate boundaries of the RIV region based on the data reported by Sareen et al. (2018b). This type of response is common in forced resonant systems and is known as a resonant horn (Arnol'd, 1977). For example, it has also been observed for flow past a circular cylinder under transverse forcing (e.g., Karniadakis and Triantafyllou, 1989; Leontini et al., 2006).

Please cite this article as: A. Sareen, J. Zhao, J. Sheridan et al., Large amplitude cross-stream sphere vibration generated by applied rotational oscillation. Journal of Fluids and Structures (2019), https://doi.org/10.1016/j.jfluidstructs.2019.03.025.

6. Conclusions

In this study, the phenomenon of *Rotary-Induced Vibration* (RIV) was investigated experimentally. Despite some similarities, it was found to be different from the classical galloping phenomenon known for asymmetric bluff bodies. Unlike the galloping response that is observed for high flow velocities, RIV was observed over $3 < U^* < 20$, which also covers the entire fundamental modes I & II synchronisation regimes, where resonance/VIV is observed in the absence of imposed rotary oscillation. The RIV response exhibited the sphere vibrations as well the total transverse lift force both being locked to the forcing frequency for the entire U^* range.

RIV was found to be driven by the effect of imposed rotary oscillation as well as associated vortex shedding. The rotary motion induces an oscillatory transverse Magnus force on the sphere. In essence, RIV is an amalgamation of the combined effects of the vortex force due to natural vortex shedding as well as or combined with vortex shedding associated with the release of vorticity as the body oscillates rotationally, along with the potential Magnus force, which is essentially due to varying bound vorticity. Depending on system parameters, the contribution of these forces to RIV changes, although during RIV the rotational phase and displacement signals remain locked.

Based on the experiments, a region was mapped out in $\alpha_R - f_R$ parameter space, where RIV is observed for the experimentally captured reduced velocity range of $3 < U^* < 20$. In view of energy extraction applications, the optimum case would be when the rotary oscillation is imposed in such a way that it matches the system frequency, where the resonant effect is greatest. Of course, for energy extraction, one would have to consider if the extra energy input is more than matched by the energy output. However, for control applications, other parameter choices can, of course, provide vibration suppression.

Acknowledgements

Anchal Sareen acknowledges the support by Australian Research Council Discovery Project grants: DP150102879 and DP170100275, as well as financial support from a Monash University (Australia) Postgraduate Publication Award (PPA).

References

Arnol'd, V.I., 1977. Loss of stability of self-oscillations close to resonance and versal deformations of equivalent vector fields. Appl. Funct. Anal. 11, 85–92.
Assi, G.R.S., Bearman, P., Meneghini, J.R., 2010. On the wake-induced vibration of tandem circular cylinders: the vortex interaction excitation mechanism. J. Fluid Mech. 661, 365–401.
Barrero-Gil, A., Pindado, S., Avila, S., 2012. Extracting energy from vortex-induced vibrations: a parametric study. Appl. Math. Model. 36, 3153–3160.
Blevins, R.D., 1990. Flow-Induced Vibration, second ed. Krieger Publishing Company, Malabar.
Choi, H., Jeon, W., Kim, J., 2008. Control of flow over a bluff body. Annu. Rev. Fluid Mech. 40, 113–139.
Du, L., Sun, X., 2015. Suppression of vortex-induced vibration using the rotary oscillation of a cylinder. Phys. Fluids 27, 023603.
Gabbai, R.D., Benaroya, H., 2005. An overview of modeling and experiments of vortex-induced vibration of circular cylinders. J. Sound Vib. 282, 575–616.
Govardhan, R., Williamson, C.H.K., 2000. Modes of vortex formation and frequency response of a freely vibrating cylinder. J. Fluid Mech. 420, 85–130.
Govardhan, R.N., Williamson, C.H.K., 2005. Vortex-induced vibrations of a sphere. J. Fluid Mech. 531, 11–47.
Karniadakis, G.E., Triantafyllou, G.S., 1989. Frequency selection and asymptotic states in laminar wakes. J. Fluid Mech. 199, 441–469.
Khalak, A., Williamson, C.H.K., 1999. Motions, forces and mode transitions in vortex-induced vibrations at low mass-damping. J. Fluids Struct. 13, 813–851.
Leontini, J.S., Stewart, M.C., Hourigan, K., 2006. Wake state and energy transitions of an oscillating cylinder at low reynolds numbers. Phys. Fluids 18, 067101–1–9.
Lighthill, J., 1986. Fundamentals concerning wave loading on offshore structures. J. Fluid Mech. 173, 667–681.
Nemes, A., Zhao, J., Lo Jacono, D., Sheridan, J., 2012. The interaction between flow-induced vibration mechanisms of a square cylinder with varying angles of attack. J. Fluid Mech. 710, 102–130.
Païdoussis, M.P., Price, S., De Langre, E., 2010. Fluid-Structure Interactions: Cross-Flow-Induced Instabilities. Cambridge University Press.
Rubinow, S., Keller, J.B., 1961. The transverse force on a spinning sphere moving in a viscous fluid. J. Fluid Mech. 11, 447–459.
Sareen, A., Zhao, J., Lo Jacono, D., Sheridan, J., Hourigan, K., Thompson, M.C., 2018a. Vortex-induced vibration of a rotating sphere. J. Fluid Mech. 837, 258–292.
Sareen, A., Zhao, J., Sheridan, J., Hourigan, K., Thompson, M.C., 2018b. The effect of imposed rotary oscillation on the flow-induced vibration of a sphere. J. Fluid Mech. 855, 703–735.
Sareen, A., Zhao, J., Sheridan, J., Hourigan, K., Thompson, M.C., 2018c. Vortex-induced vibrations of a sphere close to a free surface. J. Fluid Mech. 846, 1023–1058.
Sarpkaya, T., 2004. A critical review of the intrinsic nature of vortex-induced vibrations. J. Fluids Struct. 19, 389–447.
Soti, A.K., Zhao, J., Thompson, M.C., Sheridan, J., Bhardwaj, R., 2018. Damping effects on vortex-induced vibration of a circular cylinder and implications for power extraction. J. Fluids Struct. 81, 289–308.
Wang, Z., Du, L., Zhao, J., Sun, X., 2017. Structural response and energy extraction of a fully passive flapping foil. J. Fluids Struct. 72, 96–113.
Williamson, C.H.K., Govardhan, R., 2004. Vortex-induced vibrations. Annu. Rev. Fluid Mech. 36, 413–455.
Wong, K.W.L., Zhao, J., Lo Jacono, D., Thompson, M.C., Sheridan, J., 2017. Experimental investigation of flow-induced vibration of a rotating circular cylinder. J. Fluid Mech. 829, 486–511.
Wong, K.W.L., Zhao, J., Lo Jacono, D., Thompson, M.C., Sheridan, J., 2018. Experimental investigation of flow-induced vibrations of a sinusoidally rotating circular cylinder. J. Fluid Mech. 848, 430–466.
Zhao, J., Hourigan, K., Thompson, M.C., 2018a. Flow-induced vibration of d-section cylinders: an afterbody is not essential for vortex induced vibration. J. Fluid Mech. 851, 317–343.

Please cite this article as: A. Sareen, J. Zhao, J. Sheridan et al., Large amplitude cross-stream sphere vibration generated by applied rotational oscillation. Journal of Fluids and Structures (2019), https://doi.org/10.1016/j.jfluidstructs.2019.03.025.

Zhao, J., Hourigan, K., Thompson, M.C., 2019a. Dynamic response of elliptical cylinders undergoing transverse flow-induced vibration. J. Fluids Struct. http://dx.doi.org/10.1016/j.jfluidstructs.2019.01.011.
Zhao, J., Hourigan, K., Thompson, M.C., 2019b. An experimental investigation of flow-induced vibration of high-side-ratio rectangular cylinders. J. Fluids Struct. http://dx.doi.org/10.1016/j.jfluidstructs.2019.01.021.
Zhao, J., Leontini, J.S., Lo Jacono, D., Sheridan, J., 2014a. Chaotic vortex induced vibrations. Phys. Fluids 26, 121702.
Zhao, J., Leontini, J.S., Lo Jacono, D., Sheridan, J., 2014b. Fluid–structure interaction of a square cylinder at different angles of attack. J. Fluid Mech. 747, 688–721.
Zhao, J., Lo Jacono, D., Sheridan, J., Hourigan, K., Thompson, M.C., 2018b. Experimental investigation of in-line flow-induced vibration of a rotating cylinder. J. Fluid Mech. 847, 664–699.

Please cite this article as: A. Sareen, J. Zhao, J. Sheridan et al., Large amplitude cross-stream sphere vibration generated by applied rotational oscillation. Journal of Fluids and Structures (2019), https://doi.org/10.1016/j.jfluidstructs.2019.03.025.